# Analysis of atomic ordering of the ferromagnetic $Co_2Fe(Ga_{0.5}Ge_{0.5})$ Heusler compound using spectroscopic ellipsometry

D. Kral,[1] P. Cejpek,[1] J. Kudrnovsky,[2,*] V. Drchal,[2] L. Beran,[1] E. Vilanova,[3] G. Jakob,[3] J. Zazvorka,[1] R. Antos,[1] J. Hamrle,[1] and M. Veis[1,†]

[1]*Faculty of Mathematics and Physics, Charles University, Ke Karlovu 5, 12116 Prague, Czech Republic*
[2]*Institute of Physics of the Czech Academy of Sciences, Na Slovance 1999/2, 180 00 Prague, Czech Republic*
[3]*Institute of Physics, Johannes Gutenberg University Mainz, Staudinger Weg 7, 55099 Mainz, Germany*

(Received 3 January 2022; revised 4 August 2022; accepted 25 August 2022; published 13 October 2022)

Atomic ordering of ferromagnetic alloys, such as Heusler compounds, vastly influences their magnetic properties and overall usability. However, in some cases x-ray diffraction cannot unambiguously determine the correct atomic structure, which hampers further research. In this paper, we analyze the atomic ordering using spectroscopic ellipsometry—a simple tabletop method that researchers can use *in situ* during sample deposition. The $Co_2Fe(Ga_{0.5}Ge_{0.5})$ Heusler compound was chosen for the analysis, as the atomic ordering greatly influences its spin-polarizing capabilities. The ellispometric results are confronted with x-ray diffraction and with the help of *ab initio* calculations the qualitative changes in the optical response are linked to the changes in atomic ordering.

DOI: 10.1103/PhysRevB.106.144102

## I. INTRODUCTION

In the past three decades, ferromagnetic Heusler compounds [1,2] have gained a significant amount of attention in a vast number of research fields. Owing to their extremely flexible electronic structure, their possible utilization spans from magnetic shape memory technology [3–5] to topological insulators [6–8]. Because of the half-metallic character of certain Co-based Heusler compounds, these materials have also been investigated due to their application potential in the rapidly evolving field of spintronics [9]. Detailed research [10] has led to the development of a unique half-metallic ferromagnet, $Co_2Fe(Ga_{0.5}Ge_{0.5})$ (CFGG).

The electron structure of CFGG allows for spin polarization of up to 93% at 10 K, which is approximately 20% higher than in other Co-based Heusler compounds [11]. Moreover, CFGG stays highly spin polarized even at room temperatures, being 84% at 290 K [12]. High spin polarization is a material property necessary for proper functionality of most spintronic devices, including current-perpendicular-to-plane giant magnetoresistance pseudo spin valves (CPP-GMR PSVs) [13–17]. CFGG-based CPP-GMR PSVs give a magnetoresistance ratio of 183% at 10 K [16] making them possible successors to magnetic tunnel junctions. CFGG has also found use as a component of the all-metallic lateral spin valves (LSVs). LSVs can be used as reading heads in 0.3 Tbit/cm$^2$ magnetic recording systems and their design provides less spin torque noise in comparison to CPP-GMR PSVs. Takahashi *et al.* [18] had investigated CFGG as a possible spin-polarized electron source and reported a spin signal of 12.8 mW for CFGG-based LSVs at room temperature.

As is the case of most Heusler compounds, the remarkable properties of CFGG are vastly influenced by its crystallographic ordering [19]. In CFGG, four types of ordered structures can be present: $A2$, $B2$, $D0_3$, and $L2_1$. Only $L2_1$- and $B2$-ordered CFGG exhibits half-metallic properties; $A2$ and $D0_3$ phases are therefore undesired from the application point of view. In literature, $L2_1$ is referred to as the Heusler structure, while $A2$, $B2$, and $D0_3$ are often classified as atomic disorders [20–22].

Postdeposition annealing is a common way of inducing atomic order in Heusler compounds. After deposition at 700 K, CFGG tends to be $A2$ ordered and $B2$ or $L2_1$ ordering is achieved through annealing above 800 K [11]. At these temperatures, however, $D0_3$ ordering (Co atoms randomly swapping sites with Fe in the Heusler structure) begins to play a considerable role as well [19]. Due to the similar form factor of the antisites, $D0_3$ ordering is virtually indistinguishable from $L2_1$ ordering using standard x-ray diffraction (XRD). Therefore, the investigation of atomic ordering in CFGG remains a challenge as it requires synchrotron facilities to succeed.

Recent studies of semiconductors suggest that changes in electronic structure caused by heat treatment are directly observable in the spectral dependence of the dielectric function [23,24]. Spectroscopic ellipsometry has been employed to probe the electronic structure and investigate the transition from an amorphous to a crystalline state.

Various atomic ordering also results in a slightly different electronic structure of Heusler compounds around Fermi energy [25,26]. These differences may change the value of spin polarization, net magnetic moment, or electric conductivity. Since the optical properties of material are defined by its band

*Deceased.
†veis@karlov.mff.cuni.cz

 

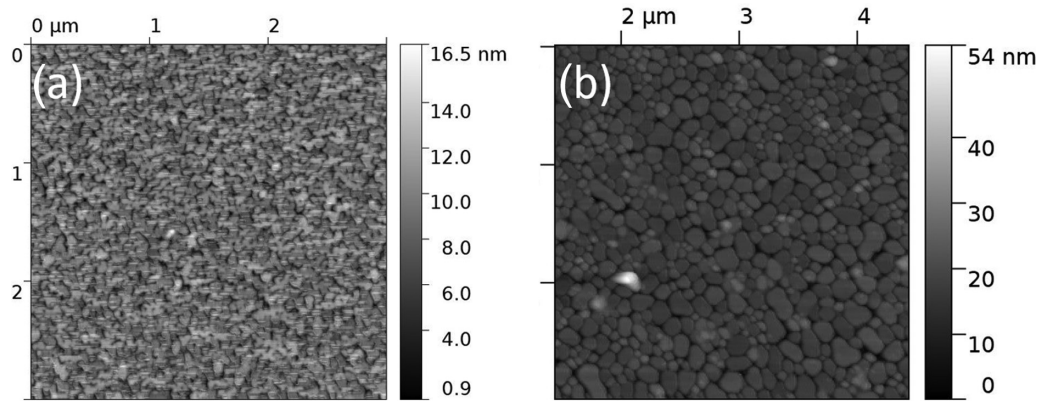


FIG. 1. Atomic force microscopy scan of a CFGG sample deposited at (a) 900 K and (b) 1200 K. The initial labyrinthlike structure breaks into separate columns with higher deposition temperature. The right-hand axis represents the height of the surface structures in nanometers.

structure [27], a variation in atomic order should project itself as a change in optical response.

This implies the possibility to utilize spectroscopic ellipsometry and systematically investigate the amount of various ordered structures in CFGG. The advantage of ellipsometry is the relatively simple *in situ* implementation for monitoring the development of atomic ordering during the deposition process and following postdeposition annealing.

In this work, we have systematically studied the optical properties of CFGG thin films deposited at various temperatures in a broad spectral range (0.7–6.5 eV). With the help of *ab initio* calculations, we link changes in the optical properties of the investigated samples to changes in their electronic structure due to the presence of different atomic orders.

## II. EXPERIMENTAL DETAILS

Nominally 20-nm-thick films of epitaxial CFGG were deposited on a (100) MgO substrate using an ultrahigh-vacuum DC magnetron sputtering system in Ar atmosphere at $4 \times 10^{-2}$ mbar. In order to achieve various types of atomic ordering, the samples were deposited at temperatures ranging from 900 to 1200 K. As was later confirmed by XRD, the atomic ordering of the samples changes with deposition temperature. To prevent oxidation, the CFGG films were capped with a 3-nm-thick Pt layer.

The samples were structurally characterized by x-ray reflectivity (XRR) and XRD using a Rigaku SmartLab diffractometer equipped with a rotating copper anode and a HyPix 3000 two-dimensional detector. Their optical properties were investigated by spectroscopic ellipsometry. The spectral dependence of the ellipsometric parameters $\psi$ and $\Delta$ was measured for each sample using an RC2 Woollam ellipsometer with dual rotating compensators. The measurements were done in reflection mode at angles of incidence of 55°, 60°, and 65° in the photon energy range from 0.7 to 6.5 eV at room temperature. The dielectric function was obtained by fitting the experimental data using the WOOLLAM COMPLETEEASE proprietary software. The atomic force microscopy (AFM) scans were carried out using a WITec Alpha 300 microscope.

*Ab initio* calculations of the density of states (DOS) have been performed using the Green's function formulation of the tight-binding linear muffin-tin orbital (TB-LMTO) method [28]. The Heusler phase (cubic $L2_1$ structure) was assumed to have $a = 0.5736$ nm [29]. The other phases ($B2$ and $D0_3$) have different occupation of lattice sites, but we assumed the same lattice constant as for $L2_1$. Random occupation of the Ga/Ge site was treated using the coherent potential approximation.

## III. RESULTS AND DISCUSSION

AFM scans of the sample surface are displayed in Fig. 1. The scans revealed labyrinth-like patterns on the surface of the samples deposited at lower temperatures (in agreement with [19]). When increasing the deposition temperature, the surface starts to break into columns that can be up to 20 nm high.

The XRR data measured on all samples are shown in the Supplemental Material [30] (Fig. S1). The measured reflectivity profiles were fitted using a theoretical model of a multilayered structure containing rough interfaces (for more details, see [31]). The fitting procedure utilized the Levenberg-Marquardt algorithm applied on the logarithm of intensities and the fitted parameters were adjusted to achieve the best agreement with experimental data. The resulting parameters are listed in Table I.

The results suggest lower quality of the Pt capping layer, since the roughness of the interfaces air-Pt and Pt-CFGG is in the same range as the thickness of the Pt layer. Moreover, the resulting relative electron density is lower than one which points to the possible presence of porosity or holes in the capping layer. This is in agreement with the AFM measurements which also revealed high roughness of the sample surface (interface air-Pt) and its columnar character. The thicknesses of the CFGG layers are close to their nominal values (approximately 20 nm).

The XRD $\theta$-$2\theta$ measurements showing (200) and (400) reflections together with the in-plane (111) scan for all investigated samples are shown in Fig. 2. The evolution of the amplitude of all diffraction peaks is clearly visible, especially for (111) diffraction. This clearly shows the change in the atomic ordering with deposition temperature and will be discussed in following paragraphs with respect to ellipsometric analysis.

TABLE I. The parameters of individual multilayers resulting from the XRR fit. $T_{Pt}$, thickness of the Pt capping layer; $T_{CFGG}$, thickness of the CFGG layer, and $\sigma_{air\text{-}Pt}$, $\sigma_{Pt\text{-}CFGG}$, and $\sigma_{CFGG\text{-}sub}$ the roughnesses of the individual interfaces defined as the root-mean-square deviation from the average position (in the vertical direction) of the interface.

| Dep. temperature (K) | $T_{Pt}$ (nm) | $T_{CFGG}$ (nm) | $\sigma_{air\text{-}Pt}$ | $\sigma_{Pt\text{-}CFGG}$ | $\sigma_{CFGG\text{-}sub}$ |
|---|---|---|---|---|---|
| 1200 | 1.1 | 18.0 | 1.8 | 0.6 | 1.3 |
| 1100 | 1.5 | 18.7 | 1.3 | 0.1 | 1.4 |
| 1000 | 1.4 | 19.1 | 0.4 | 0.6 | 1.4 |
| 900 | 0.5 | 15.7 | 1.5 | 0.4 | 1.1 |

In order to deduce the spectral dependence of the dielectric function from the ellipsometric data, we considered a model structure consisting of the following layers: An MgO substrate, a CFGG layer, and a mixed layer of CFGG, Pt, and air that represents the surface of the sample. In the last layer, the components are intermixed using Bruggeman's approach to the effective medium approximation. The content of CFGG in the surface layer was fixed at 50%, while the content of Pt was estimated from the AFM-determined roughness of the sample and the nominal thickness of the Pt layer. The optical constants of the MgO substrate and the Pt capping layer were taken from literature [32,33].

First, the spectral dependence of the dielectric function of CFGG was calculated from the experimental results using *B*-spline interpolation, and its imaginary part is displayed in Fig. 3. A marginal shift in the energy of one of the local maxima in the imaginary part of the dielectric function was observed; as the deposition temperature rises, the local maximum shifts towards higher photon energies and broadens (see Fig. 3). In order to qualitatively describe this phenomenon, a set of mathematical approaches was used to parametrize the optical response of the samples (Fig. 4). The experimental spectra of $\Psi$ and $\Delta$ together with the fitted data are shown in the Supplemental Material [30] (Fig. S2). The fit describes the experimental data well for all investigated samples.

Optical properties in the near-infrared region were described by the Drude model [34] (represented by optical conductivity $\sigma_{DC}$ and mean scattering time $\tau$), which accounts for the optical response of free charge carriers. The dependence of free electron contribution to permittivity $\varepsilon$ on photonic energy can be expressed by

$$\varepsilon(E) = \frac{-\hbar^2 \sigma_{DC}}{\varepsilon_0(\tau E^2 + i\hbar E)}.$$

Interband transitions which exhibited themselves as local extrema in the spectral dependence of the dieletric function were described by Tauc-Lorentzian oscillators, represented by transition energy $E_0$, amplitude $A$, full width at half maximum $C$, and band-gap energy $E_g$. Within this approach, the imaginary part of $\varepsilon$ above the band gap can be expressed by the following equation:

$$\varepsilon(E) = \frac{1}{E} \frac{AE_0C(E - E_g)^2}{\left(E^2 - E_0^2\right)^2 + C^2E^2}.$$

The Tauc-Lorentz approach is commonly used for semiconductors as it reflects absorption of materials in the vicinity of a defined energy band gap. Since CFGG exhibits half-metallic behavior, the optical properties originating from electronic transitions in the minority spin channel should be described using this approach.

The model parameters along with thicknesses of the layers were fitted to the experimentally determined values of $\psi$ and $\Delta$. The initial values of layer thicknesses were taken from the results of XRR. The initial values of the interband transition energies of the electronic transitions, taken from the calculated DOS of the distinctively ordered CFGG. The total DOS for $L2_1$-, $B2$-, and $D0_3$-ordered CFGG are shown in

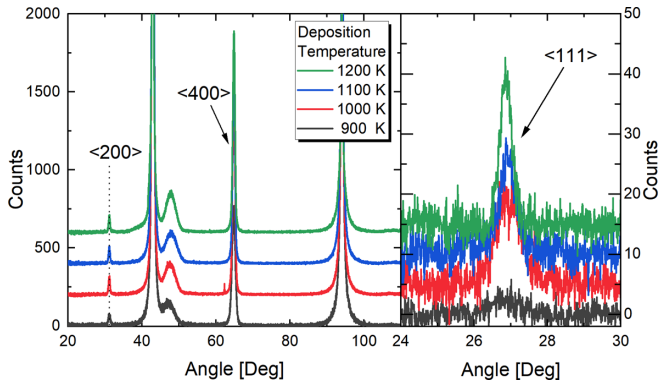


FIG. 2. XRD $\theta$-$2\theta$ measurements for all the investigated samples with highlighted (200), (400), and in-plane (111) reflections.

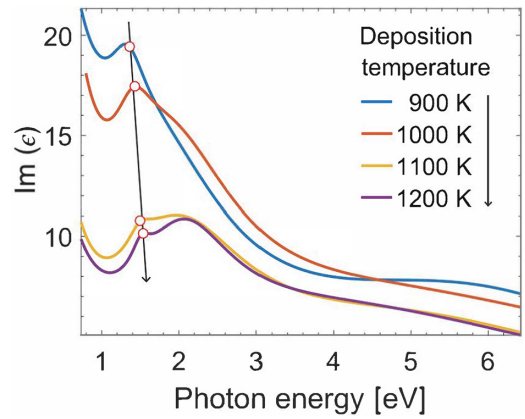


FIG. 3. Spectral dependence of the imaginary part of the dielectric function of CFGG calculated from the experimental results using a combination of Drude and Tauc-Lorentz models. The black arrow symbolizes the increase of deposition temperature of the investigated samples.

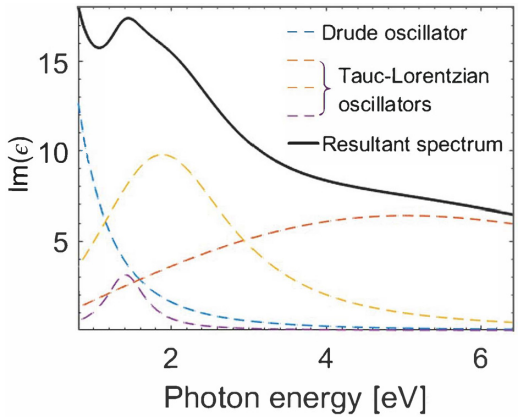


FIG. 4. The optical response of a CFGG sample deposited at 1000 K decomposed into individual oscillators. The experimentally determined dielectric function (full line) can be divided into contributions of four independent terms (dashed lines): The Drude term, representing the influence of free electrons, and three Tauc-Lorentzian oscillators resulting from minority-spin channel optical transitions.

Fig. 5. In the semiclassical theory of light-matter interaction the spectral dependence of Im($\epsilon$) arising from the single-electron transition across energy difference is proportional to the joint density of states (jDOS). This physical quantity is a combined density of the pair of energy states, initial and final. The common approach to quantitatively explain in detail all spectral structures in the optical response of materials is to calculate the jDOS and afterwards $\epsilon$ [35–38]. However, the *ab initio* TB-LMTO code, which can handle various atomic orderings without the necessity of a supercell approach, did not allow for this procedure. Therefore we limit ourselves to only a qualitative description of the changes in optical response with respect to the main DOS features for different atomic orderings. The detailed link between the electronic structure and optical properties is beyond the scope of this paper.

The calculated total DOS implies metalliclike behavior of the majority spin electrons regardless of the atomic ordering of CFGG (this fact was accounted for by the Drude term in the ellipsometric model). However, in the minority-spin channel the total DOS differs significantly for various atomic orderings. For the $B2$ and $L2_1$ orderings, Fermi energy lies in an energy gap, making the material half-metallic. While the band gap induced by the $L2_1$ ordering is approximately 0.14 eV wide, the width of the band gap originating from the $B2$ order is 0.10 eV. Since there are only few extrema in the DOS for the minority spins located below Fermi energy within the relatively narrow energy region of 2–2.5 eV, and with respect to the energy of the main spectroscopic structures in the spectral dependence of the imaginary part of dielectric function (1.5–2 eV), one could expect two distinguishable electronic transitions in the minority-spin channel. These transitions are described by the Tauc-Lorentzian terms in the ellipsometric model. Due to the presence of $B2$ ordering in all samples, the Tauc-Lorentzian terms share a common absorption edge at 0.10 eV. Figure 5 further demonstrates the fully metallic character of the $D0_3$-ordered CFGG, as the $D0_3$ structure

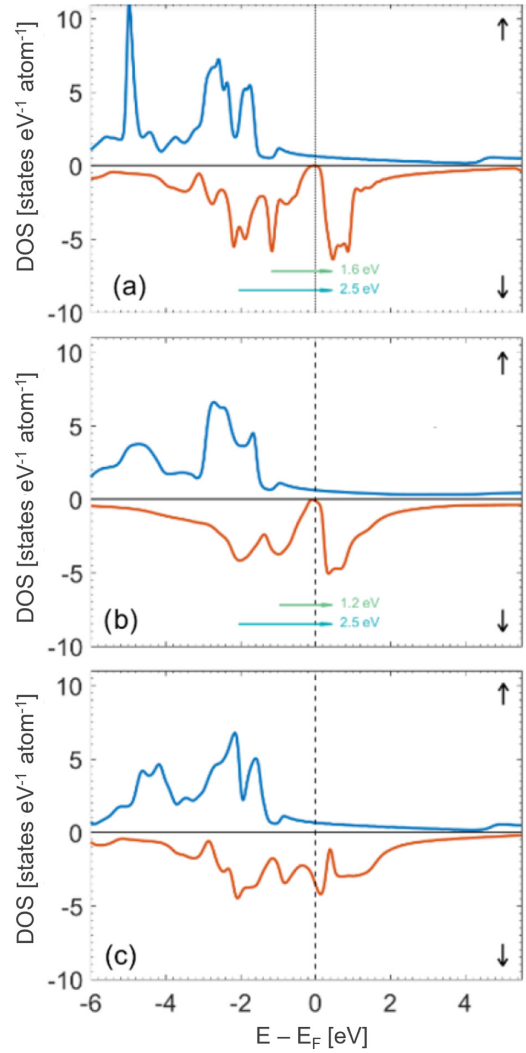


FIG. 5. The total DOS calculated for CFGG in three different atomic orderings: (a) $L2_1$, (b) $B2$, and (c) $D0_3$. The upper part of the plots represents the majority-spin channel, while the lower part represents the minority-spin channel. The possible spin-down electronic transitions are denoted by green and blue arrows. The dashed line marks the position of the Fermi level.

completely suppresses the band gap in the minority-spin channel.

Based on the *ab initio* calculations, one can argue that the transformation from full $B2$ ordering to full $L2_1$ ordering would result in a shift in energy of one of the electronic transitions by approximately 0.4 eV (see Fig. 5). We have deduced the energy of the lower-energy Tauc-Lorentzian term $E_0$ and found that it rises monotonically with increasing deposition temperature (as listed in Table II). The overall shift in the energy is approximately 0.16 eV. Moreover, the *ab initio* calculations show that in the case of $D0_3$ ordering the energy gap in the minority-spin channel closes, which would apparently increase the DC conductivity of the material. Extracting the DC conductivity $\sigma_{DC}$ from the Drude term revealed its dependence on the deposition temperature of the samples. The values alternate between 9 and 30 S m$^{-1}$ as listed in Table II.

TABLE II. XRD peaks $I_{(111)}/I_{(200)}$ ratio compared to the energy of the electronic transition $E_0$ and DC conductivity $\sigma_{DC}$ for CFGG samples deposited at temperatures ranging from 900 to 1200 K.

| Dep. temp. (K) | $I_{(111)}/I_{(200)}$ (arb. units) | $E_0$ (eV) | $\sigma_{DC}$ (S m$^{-1}$) |
|---|---|---|---|
| 900 | 0.22 | 1.36 | 17.25 |
| 1000 | 0.14 | 1.41 | 29.92 |
| 1100 | 0.12 | 1.50 | 12.05 |
| 1200 | 0.03 | 1.52 | 9.37 |

$\sigma_{DC}$ reaches a maximum at 1000 K and then drastically decreases.

The analysis of the integrated intensities of specific Bragg reflections was performed to determine the amount of $L2_1$-, $B2$-, and $D0_3$-ordered phases in the samples. As was already mentioned above, XRD cannot unambiguously distinguish between the $D0_3$ and $L2_1$ ordering in CFGG. In our case, the $D0_3$ ordering lies in the random exchange of Co and Fe atoms in the $L2_1$ lattice. The different symmetry of $D0_3$ and $L2_1$ still provides a nonvanishing 111 diffraction peak in the XRD pattern. On the other hand, the symmetry of $B2$ ordering leads to the extinction of Bragg reflection (111). Hence, the ratio of integrated intensities $I_{(111)}$ and $I_{(200)}$ is proportional to the ratio of the amount of the $L2_1$- and $D0_3$-ordered phases to the amount of $B2$ phase present in the sample.

The XRD results have therefore revealed that the content of the$L2_1$- and $D0_3$-ordered phases rises monotonically with the deposition temperature (Table II). As the deposition temperature increases, the CFGG samples become more $L2_1$- and $D0_3$-ordered at the expense of the $B2$ phase.

In Fig. 6 we qualitatively compare the temperature evolution of $I_{(111)}/I_{(200)}$ with the temperature evolution of the quantities $E_0$ and $\sigma_{DC}$ extracted from spectroscopic ellipsometry. As the deposition temperature rises, the content of the $B2$ phase starts to decrease resulting in an increase of $I_{(111)}/I_{(200)}$. The $E_0$ is following a similar trend since the $L2_1$-ordered

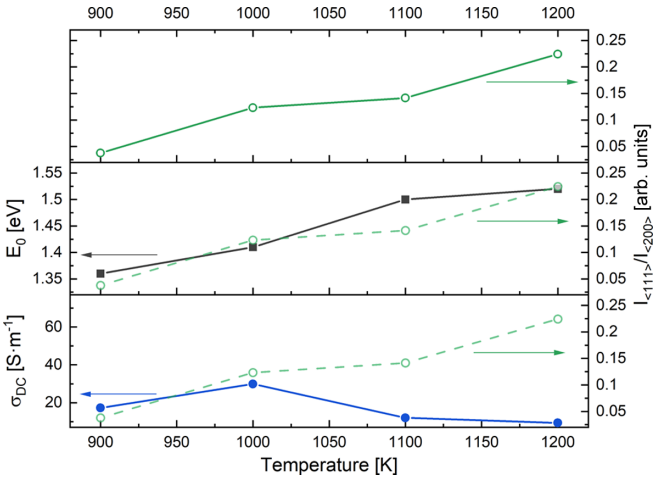


FIG. 6. Temperature evolution of the $I_{(111)}/I_{(200)}$ XRD intensities (top panel) compared with the temperature evolution of the transition energy $E_0$ (middle panel) and the DC conductivity $\sigma_{DC}$ (bottom panel).

CFGG should exhibit a larger gap in DOS for minority spins. While the transition energy rises almost linearly, the XRD peaks ratio exhibits a plateau at 1100 K. Such behavior can be explained by the temperature evolution of $\sigma_{DC}$ and so the $D0_3$ phase, showing the maximum at 1000 K. For higher temperatures the $D0_3$ phase starts to be suppressed, resulting in a decrease of the XRD peaks ratio even if the volume of the $L2_1$ phase still grows. Table II summarizes our results in a numerical form.

Both the XRD and the spectroscopic ellipsometry results show that the amount of $L2_1$ordering rises with the deposition temperature of the CFGG samples, which is in agreement with previous reports [19]. Additionally, spectroscopic ellipsometry allowed one to separate potential contributions from the $D0_3$ and $L2_1$ orderings and showed nonmonotonous dependence of the $D0_3$ ordering on temperature. Comparing the temperature-dependent trends in XRD and the ellipsometry results in Fig. 6, one can see reasonable agreement for the suggested explanation. Here we have to note that for a metallic-like material, such as CFGG, the penetration depth of the incident light is only several nanometers, which makes ellipsometry a preferentially surface-sensitive method, while XRD probes the subsurface volume of the sample. Nevertheless, similar temperature-dependent behavior of the XRD and ellipsometric data clearly demonstrates the sensitivity of spectroscopic ellipsometry to various types of atomic ordering and the possibility to separate their contributions. Since the spectroscopic ellipsometry is a nondestructive technique which can be implemented in UHV chambers for *in situ* measurements, it can provide valuable information during the optimization of deposition processes.

## IV. CONCLUSION

We have investigated the changes in atomic ordering of CFGG using experimental results obtained by spectroscopic ellipsometry in combination with *ab initio* calculations. The samples were thin-film layers of CFGG deposited at temperatures ranging from 900 to 1200 K. The optical response of the investigated samples was obtained in the photon energy range from 0.7 to 6.5 eV and the spectral dependence of the dielectric function was parametrized by a combination of Drude and Tauc-Lorentz approaches. A notable energy shift of one of the spectral structures was clearly observed. The energy of associated electronic transition increased monotonically with the deposition temperature of the CFGG layers. With the help of the total DOS provided by *ab initio* calculations we have qualitatively described this phenomenon by a gradual increase of the $L2_1$-ordered phase in the investigated layers. Simultaneously, the deposition temperature influenced DC conductivity of the samples deduced from optical measurements. This phenomenon was associated with variations in the $D0_3$-ordered content, since this order results in a band-gap closure in the minority spin channel. Unlike standard XRD, spectroscopic ellipsometry was able to distinguish between the $L2_1$- and $D0_3$-ordered phases. With respect to the possibility of *in situ* implementation, this proves spectroscopic ellipsometry to be a powerful experimental tool for optimization of deposition processes.

## ACKNOWLEDGMENTS

This work was supported by the Ministry of Education, Youth and Sports of the Czech Republic within the program OP VVV "Excellent Research Teams" under Project CZ.02.1.01/0.0/0.0/15_003/0000487-MATFUN. The work of J.K. and V.D. was supported by Czech Science Foundation (Grant No. 18-07172S). The work of M.V. and J.Z. was supported by Czech Science Foundation (Grant No. 19-09882S).



[1] T. Graf, C. Felser, and S. S. P. Parkin, Simple rules for the understanding of Heusler compounds, Prog. Solid State Chem. **39**, 1 (2011).

[2] L. Wollmann, A. K. Nayak, S. S. P. Parkin, and C. Felser, Heusler 4.0: Tunable Materials, Annu. Rev. Mater. Res. **47**, 247 (2017).

[3] S. Kaufmann, R. Niemann, T. Thersleff, U. K. Rößler, O. Heczko, J. Buschbeck, B. Holzapfel, L. Schultz, and S. Fähler, Modulated martensite: Why it forms and why it deforms easily, New J. Phys. **13**, 053029 (2011).

[4] M. Veis, L. Beran, M. Zahradnik, R. Antos, L. Straka, J. Kopecek, L. Fekete, and O. Heczko, Magneto-optical spectroscopy of ferromagnetic shape-memory Ni-Mn-Ga alloy, J. Appl. Phys. **115**, 17A936 (2014).

[5] L. Beran, P. Cejpek, M. Kulda, R. Antos, V. Holy, M. Veis, L. Straka, and O. Heczko, Optical and magneto-optical studies of martensitic transformation in Ni-Mn-Ga magnetic shape memory alloys, J. Appl. Phys. **117**, 17A919 (2015).

[6] G. Chang, S.-Y. Xu, H. Zheng, B. Singh, C.-H. Hsu, G. Bian, N. Alidoust, I. Belopolski, D. S. Sanchez, S. Zhang, H. Lin, and M. Z. Hasan, Room-temperature magnetic topological Weyl fermion and nodal line semimetal states in half-metallic Heusler $Co_2TiX$ (X = Si, Ge, or Sn), Sci. Rep. **6**, 38839 (2016).

[7] S. Chadov, S.-C. Wu, C. Felser, and I. Galanakis, Stability of Weyl points in magnetic half-metallic Heusler compounds, Phys. Rev. B **96**, 024435 (2017).

[8] M. Kargarian, M. Randeria, and N. Trivedi, Theory of Kerr and Faraday rotations and linear dichroism in Topological Weyl Semimetals, Sci. Rep. **5**, 12683 (2015).

[9] M. I. Katsnelson, V. Y. Irkhin, L. Chioncel, A. I. Lichtenstein, and R. A. de Groot, Half-metallic ferromagnets: From band structure to many-body effects, Rev. Mod. Phys. **80**, 315 (2008).

[10] B. Balke, S. Wurmehl, G. H. Fecher, C. Felser, and J. Kübler, Rational design of new materials for spintronics: $Co_2FeZ$ (Z = Al, Ga, Si, Ge), Sci. Tech. Adv. Mater. **9**, 014102 (2008).

[11] S. Li, Y. K. Takahashi, T. Furubayashi, and K. Hono, Enhancement of giant magnetoresistance by $L2_1$ ordering in $Co_2Fe(Ge_{0.5}Ga_{0.5})$ Heusler alloy current-perpendicular-to-plane pseudo spin valves, Appl. Phys. Lett. **103**, 042405 (2013).

[12] Ikhtiar, S. Kasai, Y. K. Takahashi, T. Furubayashi, S. Mitani, and K. Hono, Temperature dependence of magneto-transport properties in $Co_2Fe(Ga_{0.5}Ge_{0.5})$/Cu lateral spin valves, Appl. Phys. Lett. **108**, 062401 (2016).

[13] Y. Du, B. S. D. C. S. Varaprasad, Y. K. Takahashi, T. Furubayashi, and K. Hono, (001) textured polycrystalline current-perpendicular-to-plane pseudo spin-valves using $Co_2Fe(Ga_{0.5}Ge_{0.5})$ Heusler alloy, Appl. Phys. Lett. **103**, 202401 (2013).

[14] J. Chen, T. Furubayashi, Y. K. Takahashi, T. T. Sasaki, and K. Hono, Crystal orientation dependence of band matching in all-B2-trilayer current-perpendicular-to-plane giant magnetoresistance pseudo spin-valves using $Co_2Fe(Ga_{0.5}Ge_{0.5})$ Heusler alloy and NiAl spacer, J. Appl. Phys. **117**, 17C119 (2015).

[15] J. Chen, S. Li, T. Furubayashi, Y. K. Takahashi, and K. Hono, Crystal orientation dependence of current-perpendicular-to-plane giant magnetoresistance of pseudo spin-valves with epitaxial $Co_2Fe(Ga_{0.5}Ge_{0.5})$ Heusler alloy layers, J. Appl. Phys. **115**, 233905 (2014).

[16] J. W. Jung, Y. Sakuraba, T. T. Sasaki, Y. Miura, and K. Hono, Enhancement of magnetoresistance by inserting thin NiAl layers at the interfaces in $Co_2FeGa_{0.5}Ge_{0.5}$/Ag/$Co_2FeGa_{0.5}Ge_{0.5}$ current-perpendicular-to-plane pseudo spin valves, Appl. Phys. Lett. **108**, 102408 (2016).

[17] Y. Du, T. Furubayashi, Y. K. Takahashi, Y. Sakuraba, and K. Hono, Polycrystalline CPP-GMR pseudospin valves using ⟨001⟩ textured $Co_2Fe(Ga_{0.5}Ge_{0.5})$ layer grown on a conductive $(Mg_{0.5}Ti_{0.5})O$ buffer layer, IEEE Trans. Magn. **51**, 1 (2015).

[18] Y. K. Takahashi, S. Kasai, S. Hirayama, S. Mitani, and K. Hono, All-metallic lateral spin valves using $Co_2Fe(Ge_{0.5}Ga_{0.5})$ Heusler alloy with a large spin signal, Appl. Phys. Lett. **100**, 052405 (2012).

[19] E. Vilanova Vidal, H. Schneider, and G. Jakob, Influence of disorder on anomalous Hall effect for Heusler compounds, Phys. Rev. B **83**, 174410 (2011).

[20] Z. Gercsi and K. Hono, *Ab initio* predictions for the effect of disorder and quarternary alloying on the half-metallic properties of selected $Co_2Fe$-based Heusler alloys, J. Phys.: Condens. Matter **19**, 326216 (2007).

[21] V. Ksenofontov, C. Herbort, M. Jourdan, and C. Felser, Conversion electron Mössbauer spectroscopy of epitaxial $Co_2Cr_{0.6}Fe_{0.4}Al$ thin films, Appl. Phys. Lett. **92**, 262501 (2008).

[22] Y. Miura, K. Nagao, and M. Shirai, Atomic disorder effects on half-metallicity of the full-Heusler alloys $Co_2(Cr_{1-x}Fe_x)Al$: A first-principles study, Phys. Rev. B **69**, 144413 (2004).

[23] J. He, A. Guo, W. Li, J. Mu, X. Hou, C. Xue, and X. Chou, Structural and optoelectronic properties of a-Si:H: A new analysis based on spectroscopic ellipsometry, Vacuum **146**, 409 (2017).

[24] M. Imran, A. Saleem, N. A. Khan, A. Khurram, and N. Mehmood, Amorphous to crystalline phase transformation and band gap refinement in ZnSe thin films, Thin Solid Films **648**, 31 (2018).

[25] S. Uba, A. Bonda, L. Uba, L. V. Bekenov, and V. N. Antonov, First principles calculations of intersite disorder influence on the electronic structure and X-ray magnetic circular dichroism in CoFeMnSi Heusler alloy, Int. J. Mod. Phys. C **31**, 2050109 (2020).

[26] K. Seema, N. M. Umran, and R. Kumar, Effect of disorder on electronic, magnetic, and optical properties of $Co_2CrZ$ Heusler

alloys (Z = Al, Ga, Si, Ge), J. Supercond. Novel Magn. **29**, 401 (2016).

[27] P. Y. Yu and M. Cardona, *Fundamentals of Semiconductors* (Springer Berlin, Heidelberg, 2010).

[28] I. Turek, *Electronic Structure of Disordered Alloys, Surfaces and Interfaces* (Kluwer, Dordrecht, 1997).

[29] K. R. Kumar, K. K. Bharathi, J. A. Chelvane, S. Venkatesh, G. Markandeyulu, and N. Harishkumar, First-principles calculation and experimental investigations on full-Heusler alloy $Co_2FeGe$, IEEE Trans. Magn. **45**, 3997 (2009).

[30] See Supplemental Material at http://link.aps.org/supplemental/10.1103/PhysRevB.106.144102 for detailed XRR and ellipsometric characterization.

[31] J. Als-Nielsen, *Elements of Modern X-ray Physics*, 2nd ed. (Wiley, New York, 2011).

[32] E. D. Palik, *Handbook of Optical Constants of Solids* (Elsevier, New York, 2012).

[33] E. D. Palik, *Handbook of Optical Constants of Solids* (Elsevier, New York, 1991), Vol. 2.

[34] G. E. Jellison and F. A. Modine, Parameterization of the optical functions of amorphous materials in the interband region, Appl. Phys. Lett. **69**, 371 (1996).

[35] Y. V. Kudryavtsev, N. V. Uvarov, and J. Dubowik, Optical properties of Fe-Mn-Ga alloys, J. Phys.: Condens. Matter **31**, 235501 (2019).

[36] L. Uba, A. Bonda, S. Uba, L. V. Bekenov, and V. N. Antonov, Electronic structure and magneto-optical Kerr spectra of an epitaxial $Ni_{54.3}Mn_{31.9}Sn_{13.8}$ Heusler alloy film, J. Phys.: Condens. Matter **29**, 275801 (2017).

[37] S. Uba, A. Bonda, L. Uba, L. V. Bekenov, V. N. Antonov, and A. Ernst, Electronic structure and magneto-optical Kerr effect spectra of ferromagnetic shape-memory Ni-Mn-Ga alloys: Experiment and density functional theory calculations, Phys. Rev. B **94**, 054427 (2016).

[38] D. Král, L. Beran, M. Zelený, J. Zemen, R. Antoš, J. Hamrle, J. Zázvorka, M. Rameš, K. Onderková, O. Heczko, and M. Veis, Magnetic and magneto-optical properties of $Fe_{75-x}Mn_{25}Ga_x$ Heusler-like compounds, Materials **13**, 703 (2020).